Contents list available at CBIORE journal website

International Journal of Renewable Energy Development

Journal homepage: https://ijred.cbiore.id

Research Article

Study on the effect of bionic flap based on owl wing contour on aerodynamic noise of airfoil

Xian Fan Xie[a], Liu Chen[a], Jian Shen Zhu[b*]

[a]College of Energy and Power Engineering, University of Shanghai for Science and Technology, Shanghai, 200093, China

[b]Marine Design and Research Institute of China, Shanghai,200011,China

Abstract. Modifying flap geometry to reduce trailing-edge turbulence is an effective approach to lower wind-turbine blade aerodynamic noise. Based on the NACA0018 airfoil, a new bionic serrated flap was designed by mimicking the owl wing structure. Numerical methods were employed to investigate its noise reduction mechanism, utilizing Improved Delayed Detached Eddy Simulation (IDDES) and the Ffowcs Williams-Hawkings (FW-H) method. The aerodynamic and aeroacoustic performance of the baseline airfoil, a flat-plate Gurney flap (PGF), a standard serrated flap (SGF), and the bionic flap (BGF) were calculated at different inflow wind speeds (Re = 7×104, 1.4×105 and 2.1×105) under various inflow angles (0°, 6°, 10° and 15°). Numerical results demonstrate that the proposed BGF configuration mitigates the additional noise induced by the traditional Gurney flap, with reductions observed in the overall sound pressure levels across the monitored directivity points. Compared to the baseline airfoil, the BGF demonstrates noise reduction at low angles of attack (AoA < 6°), with a peak OASPL decrease of 4.6 dB. However, this aeroacoustic advantage diminishes rapidly as the AoA exceeds 6°, suggesting that the noise-suppression effectiveness of the bionic contour is highly sensitive to the inflow angle. Analysis of wake vortex structures and turbulence intensity reveals that the curved bionic flap effectively suppresses vortex clusters and turbulence intensity, leading to reduce the airfoil's aerodynamic noise.

Keywords: Aeroacoustics; Bionic airfoil; Flow control; Wind turbine;Vortex structures

Received: 9th March 2026; Revised: 17th May 2026; Accepted: 30th June 2026; Available online: 1st July 2026

1. Introduction

Amidst the persistent strain on fossil fuel supplies and the accelerated global transition toward sustainable energy paradigms, wind energy has been widely recognized as one of the most viable and rapidly evolving renewable sources for human utilization (Chen *et al*., 2025). Owing to its vast reserves, minimal environmental impact, and inherent renewability, wind power has become a cornerstone of the future global energy infrastructure (Song *et al*., 2020; Sun *et al*., 2017). The deployment scenarios and developmental scale of wind power generation have continued to expand aggressively (Si *et al*., 2024). In the first half of 2025, the global wind power industry achieved robust growth, with newly installed capacity increasing by 64% compared to the same period in 2024. Specifically, between January and June 2025, the added capacity reached 72.2 gigawatts (GW), a significant rise from the 44.1 GW recorded in the previous year. As of June 2025, the cumulative global wind capacity† attained 1,245 GW (or 1.25 TW), reflecting an annual growth rate of 13.5%.

Despite these advancements, the aerodynamic noise issues arising from wind turbine operations have become increasingly prominent, evolving into a critical constraint for wind farm site selection, project construction, and operational permitting. For instance, the noise emitted by conventional straight-bladed wind turbines has been documented to exert deleterious effects on the reproduction and survival of fauna in the vicinity of wind farms(Piorkowski *et al*., 2012; May, 2019). Furthermore, the acoustic impact of small-scale wind turbines is often considered even more intrusive, not only because they are generally positioned closer to human habitation, but also due to their significantly higher rotational speeds when contrasted with macro-scale units. This operational characteristic results in a distinct aeroacoustic signature, manifesting as audible swishing, humming, and whistling noises across a broad frequency spectrum (Liu *et al*., 2019; Wu *et al*., 2020; Li *et al*., 2021).Therefore, reducing aerodynamic noise while maintaining aerodynamic performance has emerged as a pivotal challenge in modern wind turbine blade design. An optimally designed airfoil profile can concurrently fulfill multiple objectives, such as minimizing drag loss, enhancing circulation, and suppressing acoustic radiation.

According to Brooks *et al*. (Brooks *et al*.,1989), aerodynamic noise is identified as the result of multiple aeroacoustic mechanisms. These encompass the stochastic excitation of the blade surface by the turbulent boundary layer, alongside the complex vortical dynamics associated with flow separation and the evolution of tip-vortex structures.The resulting noise spectra typically exhibit broadband characteristics, with low-frequency components becoming

* Corresponding author
Email: chen_liu@usst.edu.cn (L. Chen)

https://doi.org/10.61435/ijred.2026.62430
ISSN: 2252-4940/© 2026.The Author(s). Published by CBIORE

more dominant as wind speed increases, which poses potential threats to the surrounding environment and local fauna. Based on Powell's vortex sound theory(Powell,1964), flow-induced noise consists of three types of acoustic sources: monopoles, dipoles, and quadrupoles. In terms of physical distribution, the blade surface is predominantly affected by monopoles and dipoles, whereas the spatial flow field is governed by dipoles and quadrupoles. If the blade is treated as a rigid, stationary boundary, the monopole term vanishes.

Having identified the noise generation mechanisms, researchers have explored various methodologies to mitigate self-generated noise, among which the Serrated Trailing Edge (STE) has proven to be one of the most effective strategies. Through theoretical modeling, Howe pointed out that the noise reduction efficacy of STE is primarily determined by its aspect ratio(Howe, 1991). Subsequent experimental studies (Chong *et al*., 2013) demonstrated that while decreasing the aspect ratio enhances noise reduction capacity, an excessively low ratio tends to induce bluntness-induced tonal noise. Avallone *et al*(Avallone *et al*., 2016). utilized PIV technology to reveal the flow-field modulation mechanism of STE: at positive angles of attack, the pressure differential across the blade induces counter-rotating vortex pairs at the serration edges. These vortex structures reshape the near-field turbulence and reduce the spanwise correlation of velocity fluctuations, thus effectively disrupting the acoustic feedback loop.

The Gurney Flap (GF) is a passive lift-enhancing structure installed on the trailing edge of an airfoil, has been a subject of intense aerodynamic research since its introduction in 1978(Wilbur *et al*., 2018). Its geometric parameters directly dictate the distributions of aerodynamic and acoustic quantities around the blade. Liu *et al*.(Liu & Montefort, 2007) confirmed that GFs significantly increase the pressure difference between the suction and pressure sides of the airfoil, thereby substantially boosting the lift coefficient. Wang *et al*. (Wang *et al*., 2008) further reported that the lift augmentation reaches its peak when the flap is mounted perpendicular to the trailing edge. Amini (Amini *et al*., 2015) studied the performance of the Gurney flap at different altitudes. However, subsequent research revealed that while the flap increases lift, it simultaneously introduces substantial drag penalties and aerodynamic noise.

To mitigate the additional noise induced by GFs, various structural modifications have been proposed, such as perforations, slits(Mayer *et al*., 2006; Yang *et al* ., 2017), and serrations (Yu *et al* ., 2022). Oerlemans *et al*. (Oerlemans *et al* ., 2022;Yang, 2025) investigated serrated Gurney flaps and found that they could reduce the drag compared to a baseline GF, though often at the cost of diminished lift enhancement. Concurrently, birds of prey such as owls have demonstrated extraordinary silent flight capabilities. Research (Kong *et al*., 2015) indicates that their unique flexible fringes and tail feather structures are key to noise suppression. Liu (Liu *et al*., 2012) employed reverse engineering to extract noise-reduction features from the non-smooth trailing-edge morphology of goshawks to establish a bionic blade model. Chen *et al*. (Chen *et al*.,2022) designed a curved trailing-edge serrated airfoil based on owl wing characteristics, which achieved significant noise reduction. The underlying mechanism involves the bionic configuration suppressing pressure pulsations near the trailing edge and attenuating turbulent fluctuations within the serration gaps.

Despite these advancements in serrated and bionic trailing edges, existing literature has focused predominantly on the bionic design of the airfoil trailing edge itself. Research regarding the bionic modification of the Gurney Flap—a classic lift-enhancement device—remains remarkably limited. In particular, the integration of bionic curved structures into flap configurations and the systematic analysis of their impact on aerodynamic efficiency, acoustic radiation, and wake vortex evolution lack in-depth investigation.

Regarding numerical modeling, while the SST k-ω model reduces computational costs for mean flow calculations, it suffers from insufficient spatial and temporal resolution, failing to meet the high-fidelity requirements of aeroacoustic computations (Colonius & Lele, 2004). Although LES is more accurate in calculating transient flow fields, thus better capturing vortices.its stringent grid requirements lead to prohibitive computational costs (Asada & Kawai, 2018). The IDDES offers a robust alternative by solving three-dimensional unsteady flows using a hybrid strategy. It leverages the advantages of both RANS and LES by applying RANS in the near-wall regions and switching to LES in regions far from the wall. This approach ensures high computational efficiency while maintaining superior accuracy over traditional RANS methods(Chen *et al*., 2020). Consequently, the present study employs the IDDES framework coupled with the Ffowcs Williams-Hawkings (FW-H) acoustic analogy to evaluate airfoils equipped with baseline GFs, standard serrated flaps (SGF), and the proposed bionic curved flaps (BGF). This work aims to analyze the influence of bionic curved flaps on aerodynamic noise, characterize the wake vortex structures, and reveal the underlying noise-reduction mechanisms, resulting in providing a theoretical foundation for airfoil optimization.

2. Mathematical and physical models

2.1 Geometric Configuration of Bionic Curved Flaps

To evaluate the influence of bionic flap configurations on the aerodynamic characteristics and aeroacoustic behavior of the airfoil, For a NACA0018 airfoil featuring a chord length of c = 70 mm as the reference configuration, the influence on

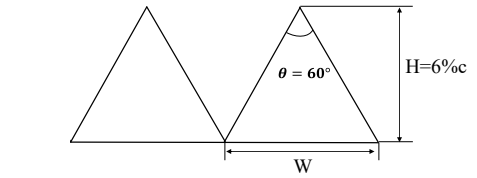

(a) Traditional triangular serrations(SGF)

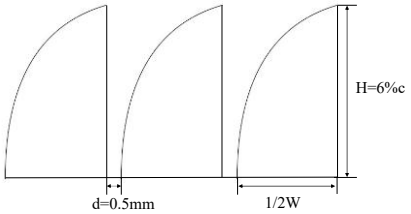

(b) Bionic curved serrations(BGF)

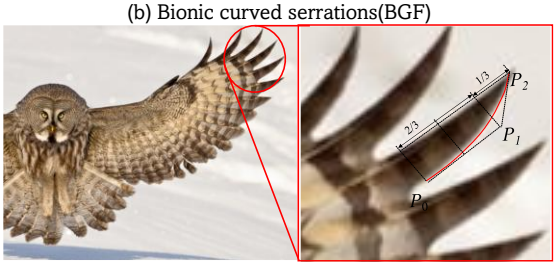

(c) Owl-wing morphology

Fig. 1. Flap serration profile

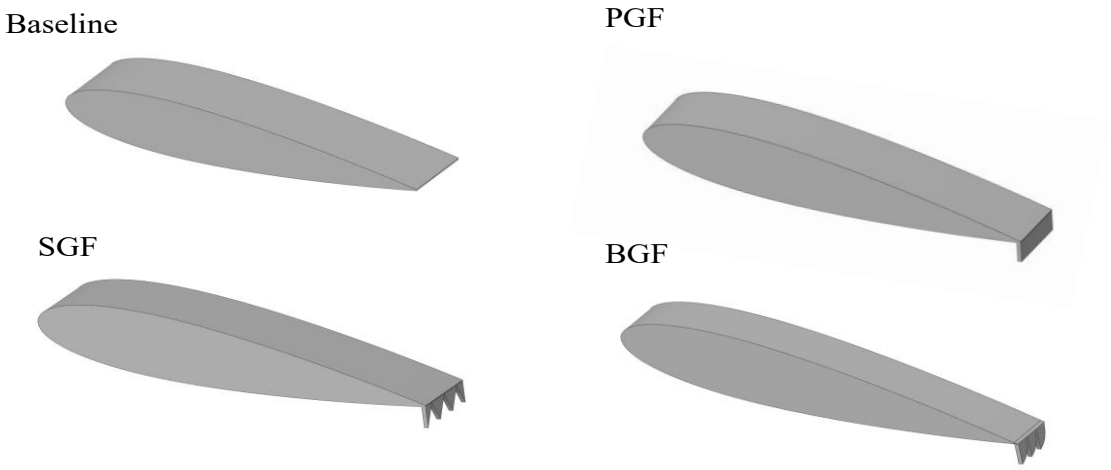

Fig.2. Airfoil with different flap configurations

aeroacoustic performance is assessed by integrating flaps with a relative height of 6% c and thickness of 1% c. The traditional Serrated Gurney Flap (SGF) is configured with uniform triangular serrations at a serration angle of θ = 60°. The proposed bionic flap configuration, inspired by the unique wing structures of owls(Wang & Liu, 2022), is designated as the Bionic Gurney Flap (BGF). The curved profile of the owl feather serrations is fitted using a second-order Bezier curve (Eq. (1)), with the fitting formula expressed as follows(Feng *et al*., 2023):

$$B(t) = P_0(1-t)^2 + 2P_1(1-t) + P_2t^2 \quad (1)$$

$$(t) = [P_0 \quad P_1 \quad P_2]\begin{bmatrix}1 & -2 & 1\\ 0 & 2 & -2\\ 0 & 0 & 1\end{bmatrix}\begin{bmatrix}1\\ t\\ t^2\end{bmatrix} \quad (2)$$

To ensure that the height of the bionic curved serrations remains consistent with that of the triangular serrations, the dimensions of the triangular serrations are substituted into Eq. (2), yielding the expression for the curved serrations as shown in Eq. (3):

$$\begin{bmatrix}x(t)\\ y(t)\end{bmatrix} = \begin{bmatrix}-2.42t^2 + 2.42\\ -2.8t^2 + 7t - 2.1\end{bmatrix} \quad (3)$$

In the formula: P0 —starting point coordinates;P_1 —curve shape control point coordinates;$P_1 = 2/3\ \overline{P_0P_2}$;P_2 —endpoint coordinates. The resulting BGF curve is shown in Fig.1.(b).

The spanwise extent for all three airfoil configurations is defined as three serration wavelengths to ensure that at least two complete serration cycles are encompassed within a single computational domain, as illustrated in Fig.2.

2.2 Computational Domain and Mesh Generation

The computational domain and import/export conditions of the model are shown in Figure.3. The computational domain features a C-type topology, with the upstream region consisting of a semicircle with a diameter of 20c, extending 15c in the streamwise direction. The inlet velocity is u_∞ = 29.2 m/s, Re = 1.4×10^5. The outlet boundary is set as a pressure outlet with a relative static pressure of 0 Pa. Given that the NACA0018 airfoil can be modeled as an assembly of spatially periodic blade segments, periodic boundary conditions are applied to the spanwise walls, while a no-slip condition is imposed on the airfoil surface. Local mesh refinement is implemented around the airfoil; The first near-wall grid layer on the airfoil surface is 1×10^{-5} m, with a geometric growth rate of 1.05 and a total of 35 boundary layers, ensuring that the dimensionless wall distance y+ is approximately 1(Yan *et al*., 2020).

2.3 Model Validation

Numerical simulations commenced with steady-state computations to establish initial conditions for the unsteady runs. The steady phase relied on the Shear Stress Transport SST k-ω model, which is well-regarded for its reliable prediction of aerodynamic loads and separation behavior under moderate adverse pressure gradients (Menter, 1994). For the time-accurate simulations, the IDDES was utilized. In this IDDES implementation, the SST k-ω model was responsible for the

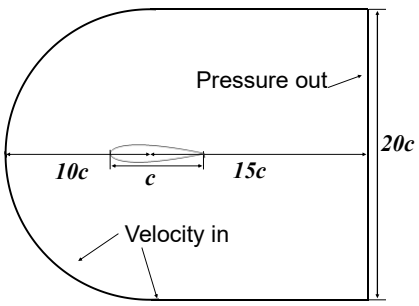

Fig.3. Computational domain

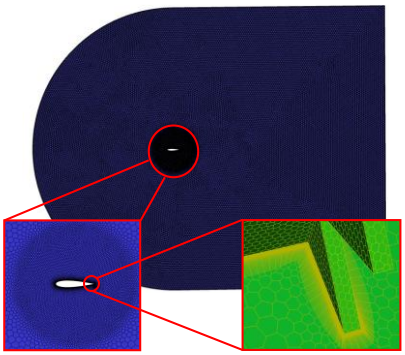

Fig.4. Flow field mesh generation

RANS (Reynolds-Averaged Navier-Stokes) zones adjacent to the wall, while the Large Eddy Simulation (LES) mode captured flow details in separated regions. By doing so, the method leverages the computational efficiency of RANS near solid boundaries and the fidelity of LES in areas with massive separation, enabling a detailed representation of transient turbulent dynamics. Their transport equations are expressed as:

$$\rho\frac{\partial k}{\partial t}+\rho\frac{\partial}{\partial x_j}(u_j k)=\frac{\partial}{\partial x_j}\left[(\mu+\mu_t\sigma_k)\frac{\partial k}{\partial x_j}\right]+P_k - \beta^*\rho\omega k \quad (4)$$

$$\rho\frac{\partial \omega}{\partial t}+\rho\frac{\partial}{\partial x_j}(u_j)=\omega\frac{\partial}{\partial x_j}\left[(\mu+\mu_i\sigma_\omega)\frac{\partial \omega}{\partial x_j}\right]+P_\omega - \beta\rho\omega^2+2(1-F_1)\frac{\rho\sigma_{\omega 2}}{\omega}\frac{\partial k}{\partial x_j}\frac{\partial \omega}{\partial x_j} \quad (5)$$

Where μ represents the dynamic viscosity and $\mu_t$is the turbulent viscosity. The terms β, β^*, $\sigma_{\omega 2}, \partial k, \partial\omega$ denote empirical coefficients specific to the SST k-ω closure. P_k and $P\omega$ represent the effective production rates of k and ω, F_1 is the correction factor

Once the unsteady flow field reached a statistically quasi-steady state, the transient pressure fluctuations on the blade surfaces were extracted as acoustic sources. Subsequently, the far-field acoustic field was determined via the FW-H acoustic analogy. This model operates on the core concept of extracting equivalent acoustic sources from the nonlinear flow field, thereby providing a precise characterization of the noise caused by fluid-structure interactions. An advantage of this method is the decoupling of flow field computation from acoustic propagation; since the two processes do not interfere, no additional acoustic mesh is required in the far-field. The equation is defined as follows:

$$\left(\frac{1}{c^2}\cdot\frac{\partial^2}{\partial t^2}-\frac{\partial^2}{\partial x_i^2}\right)p'(x_i,t) = \frac{\partial}{\partial t}\{[\rho_0 v_n+\rho(u_n-v_n)]\delta(f)\} + \frac{\partial^2}{\partial x_i\,\partial y_i}[T_{ij}H(f)] - \frac{\partial}{\partial x_i}\{[-p'_{ij}n_{ij}+\rho u_i(u_n - v_n)]\delta(f)\} \quad (6)$$

$$H(f)=\begin{cases}0, f(x_i,t)<0\\ 1, f(x_i,t)\geq 0\end{cases} \quad (7)$$

$$\delta(f)=\frac{\partial H(f)}{\partial f} \quad (8)$$

In the formula: $\frac{1}{c^2}\cdot\frac{\partial^2}{\partial t^2}-\frac{\partial^2}{\partial x_i^2}$ —— wave operator; $p'(x_i,t)$ —— far-field sound pressure.

The pressure-velocity coupling was resolved using the SIMPLEC algorithm. The spanwise correlation of turbulence and acoustic dissipation are closely linked to vortex shedding processes(Amiet,1975). Investigating their variations is crucial for elucidating the underlying noise suppression mechanisms. To quantify this, the spanwise correlation coefficient (Rpp) is introduced and defined as follows:

$$R_{PP}=\frac{\mathrm{cov}\big(P(z_1,t),P(z_2,t)\big)}{\sqrt{\mathrm{var}(P(z_1,t)\mathrm{var}\,(P(z_2,t)}} \quad (9)$$

In the formula ,cov is for covariance calculation, var is for variance calculation, and P(z,0) is the pressure value at position z at time t. To evaluate this, a series of pressure monitoring points were arranged contiguously along the spanwise direction at the airfoil trailing edge (x/c = 1.0), as illustrated in Fig.5.

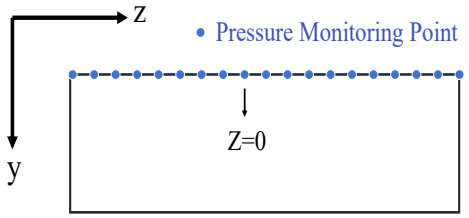

Fig.5. Monitoring Point Distribution

Turbulent Kinetic Energy (TKE) characterizes the momentum transport capacity and reflects the intensity of turbulent fluctuations. It is defined as follows:

$$\mathrm{TKE}=\bar{u_i'u_i'}/2=\frac{3}{2}(u_0 I)^2 \quad (10)$$

The aerodynamic noise of an airfoil is intimately coupled with its generated vortex structures. According to Powell's Vortex Sound Theory, for isentropic and adiabatic fluids at low Mach numbers, the sole source of the radiated acoustic field is vorticity. Powell investigated the relationship between hydrodynamic forces and noise, linking them to vortex motion to derive the mechanism and mathematical expression for vortex-induced noise (Eq. (11)):

$$\nabla^2 p_a-\frac{1}{c_0^2}\frac{\partial^2 p_a}{\partial t^2}=-\nabla\cdot\rho(\boldsymbol{\omega}\times\boldsymbol{u}) \quad (11)$$

In the formula,c_0 is the speed of sound in the far-field; $\boldsymbol{u}$ is the velocity vector;$\boldsymbol{\omega}$ is the vorticity,As indicated by Eq. (11), the magnitude of the acoustic pressure is directly governed by vortex motion; thus, mitigating vorticity is conducive to noise reduction.

To identify the vortex structures in the transient flow field, the Ω vortex identification method was employed. In complex flow fields where strong and weak vortices coexist, conventional methods often fail: a threshold that is too high obscures weak vortices, while one that is too low blurs the structural clarity. The Ω method, characterized by a normalized threshold, overcomes these limitations. The parameter Ω represents the ratio of the rotating vorticity to the total vorticity, ranging from 0 to 1. Specifically, Ω = 0 denotes irrotational motion, while Ω = 1 represents pure rotation. Following established literature(Liu, 2020) a threshold of Ω > 0.5 implies that the rotation strength exceeds the deformation rate, providing a clear physical basis for defining vortex boundaries as isosurfaces. Furthermore, following Zhang *et al.*(Zhang *et al.*, 2020), to identify vortices on specific planes in the wake, the symmetric tensor A and anti-symmetric tensor B were projected onto the XOY plane:

$$\Omega_{\mathrm{axial}}=\frac{\|B_{\mathrm{axial}}\|_F^2}{\|A_{\mathrm{axial}}\|_F^2+\|B_{\mathrm{axial}}\|_F^2+\varepsilon_{\mathrm{axial}}} \quad (12)$$

where A_{axial} and B_{axial} represent the projections of the symmetric and anti-symmetric tensors onto the XOY plane, respectively, and Ω_{axial} denotes the two-dimensional Omega vorticity.

Table 1
Grid independence verification (α = 6°)

	Grid numbers	C_L	C_D	Point A OASPL
Exp	—	0.531	0.0242	—
Mesh1	680000	0.527	0.0234	77.1
Mesh2	1400000	0.533	0.0233	77.5
Mesh3	2360000	0.538	0.0231	78.1.

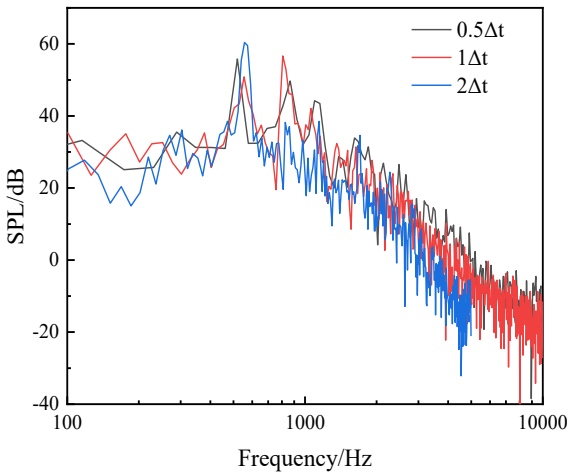

Fig.6. Time step size sensitivity ansys

The mesh independence evaluation is conducted based on the lift (C_L) and drag (C_D) coefficients of the NACA0018 airfoil at α = 6∘. Three sets of refined meshes are evaluated, with the y+ values for all cases (from coarse to fine) maintained near 1. The validation results are presented in Table 1. The deviations for C_L and C_D in Mesh 2 are 0.37% and 3.7%, and noise deviation is 0.77%. respectively. Since further increasing the mesh density yields negligible improvements in simulation accuracy, Mesh 2, representing a medium grid density, is selected for further simulations to ensure an appropriate compromise between computational expense and numerical accuracy.

To evaluate the temporal discretization sensitivity of the aeroacoustic simulations, additional calculations were performed using three different time steps: 1×10^{-4} s, 5×10^{-5} s, and 2.5×10^{-5} s. Figure.6 compares the corresponding SPL spectra at the monitoring location.The results show that the dominant spectral peaks and the overall spectral distributions obtained using 5×10^{-5} s, and 2.5×10^{-5} s remain in good agreement throughout the low- and mid-frequency ranges. In contrast, the larger time step 1×10^{-4} s exhibits noticeable attenuation in the high-frequency region, indicating insufficient temporal resolution for small-scale turbulent fluctuations.Considering both computational cost and spectral accuracy, the time step of 5×10^{-5} s was selected for the present aeroacoustic simulations. At this setting, the maximum Courant Number (Co) was calculated to be 0.487, which strictly satisfies the stability requirement of Co < 1 for unsteady numerical simulations.

The surface pressure coefficient (Cp) of the baseline airfoil at Re = 1.6×10^5 and an angle of attack (AoA) of α = 6°, as well as the C_L and C_D at various AoAs, were compared with experimental data to verify the numerical fidelity. The lift and drag coefficients, C_L and C_D, are defined as follows:

$$c_L = F_L / 0.5\rho u_0^2 S \tag{13}$$

$$c_D = F_D / 0.5\rho u_0^2 S \tag{14}$$

The pressure coefficient Cp is defined as follows:

$$C_P = \frac{2(p - p_\infty)}{\rho V_\infty^2} \tag{15}$$

Where the fluid density ρ is in kg/m³, the freestream velocity $V\infty$ in m/s, and the pressures p (local) and P_∞ (freestream) are both expressed in Pascals.

In Fig.7, The fidelity of the numerical model is confirmed by the favorable agreement between the calculated and experimental pressure distributions at α = 6°(Kim, 2006)., the computed lift and drag characteristics exhibit high consistency with Jacobs' (Jacobs, 1937)measurements. The numerical calculation results of the sound field were validated based on experiment, as shown in Table 2. The numerical calculation results of the OASPL of the airfoil under three types of grids were compared with the experimental results (Fujisawa *et al.*, 2020).

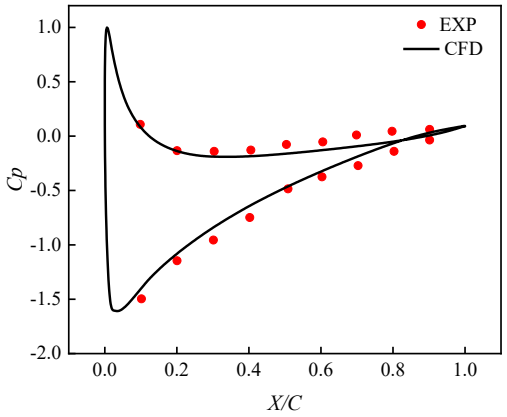

(a) Comparison of C_P between numerical results and experimental data.

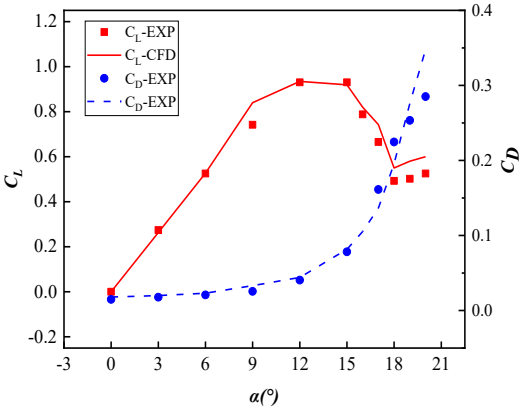

(b) Comparison of C_L *and* C_D with experimental values.

Fig.7.Validation of simulated and experimental aerodynamic characteristics

Table 2
Sound pressure levels at monitoring point (NACA0018)

monitoring point	Exp/dB	Mesh1		Mesh2		Mesh3	
		OASPL/dB	Deviation/%	OASPL/dB	Deviation/%	OASPL/dB	Deviation/%
Mic1	87.64	84.65	3.41	85.95	1.92	85.70	2.21
Mic2	87.59	84.90	3.07	85.72	2.12	85.38	2.52

3 Calculation results and analysis

3.1 Aerodynamic Performance

The aerodynamic characteristics of an airfoil are typically evaluated using the lift-to-drag ratio (C_L/C_D) and the maximum lift coefficient ($C_{L,max}$). Figure.8 shows compared with the Baseline, the $C_{L,max}$ of the airfoils equipped with PGF, SGF, and BGF increases by 78.8%, 48.7%, and 61.7%, respectively. Notably, the BGF exhibits a more significant lift enhancement compared to the SGF. While the three flap configurations improve lift, they simultaneously induce an increase in drag. It is observed that the enhancement effects on both lift and drag are positively correlated with the effective windward area of the flaps. To provide a more comprehensive evaluation of aerodynamic efficiency. Relatives to the Baseline, the maximum lift-to-drag ratio ($C_L/C_{D,max}$) for PGF, SGF, and BGF increases by 7.8%, 9.7%, and 16.8%, respectively. Furthermore, it is found that while the installation of Gurney flaps enhances the lift-to-drag ratio, it also causes the stall angle of attack to advance from 14° to 11°, indicating that premature flow separation occurs at high angles of attack.

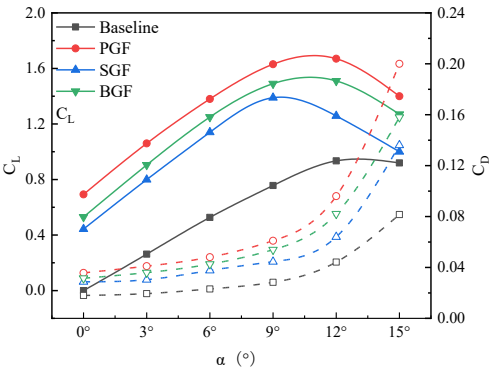

(a) Lift and drag coefficients (C_L *and* C_D) changes under different angle of attack.

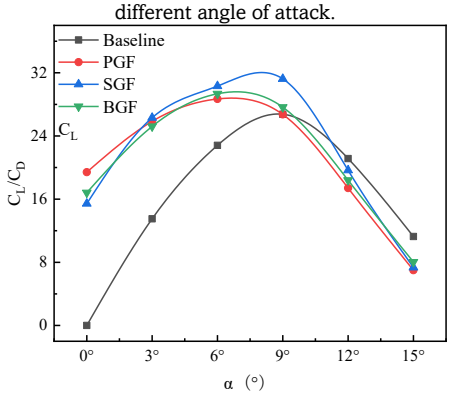

(b) Lift-to-drag ratio (C_L/C_D) changes under different angle of attack.

Fig.8. Effect of flap configuration on aerodynamic performance

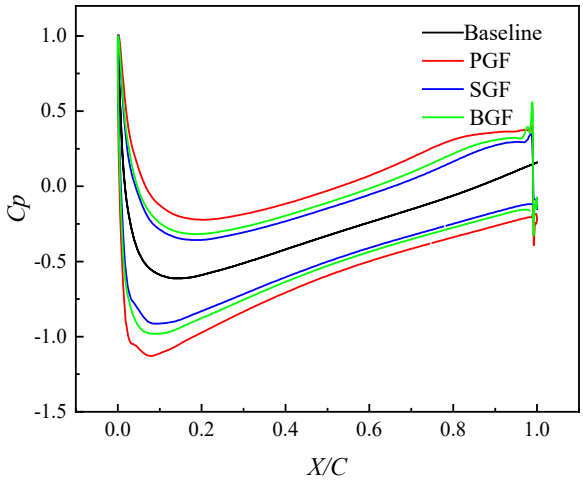

Fig.9. Pressure coefficient distribution over the airfoil surface

Fig. 9 presents the comparison of surface pressure coefficient distributions for the baseline and modified airfoils at an angle of attack of α = 0°. Since NACA0018 is a symmetrical airfoil, the pressure difference between the suction and pressure surfaces is zero when the angle of attack is 0°, resulting in a zero lift coefficient. The PGF, possessing the largest effective windward area, induces the most significant pressure differential between the pressure and suction surfaces. While the pressure distributions on the pressure surface are fundamentally consistent for both the Serrated Gurney Flap (SGF) and the Bionic Gurney Flap (BGF), the BGF exhibits lower pressure near the leading edge of the suction surface compared to the SGF. Consequently, the lift enhancement capability of the BGF is more pronounced than that of the SGF.

3.2 Aeroacoustic Characteristics

Given that the propagation of airfoil aerodynamic noise exhibits distinct directivity characteristics, a circular array of acoustic observers was established to capture the radiation pattern. As illustrated in Fig. 10, a total of 24 monitoring points were distributed at azimuthal intervals of 15° along a circumference with R = 5c, centered at the airfoil mid-chord. Among these, Monitoring Point A was selected as the primary reference location for the detailed analysis of noise spectral characteristics.

Fig.11. illustrates the directivity distributions of the OASPL for the Baseline (without flap), PGF, traditional Serrated Gurney Flap (SGF), and Bionic Gurney Flap (BGF) at angles of attack of α = 0°, 6°, 10°and 15°. For all four examined airfoil geometries, the acoustic field radiation consistently

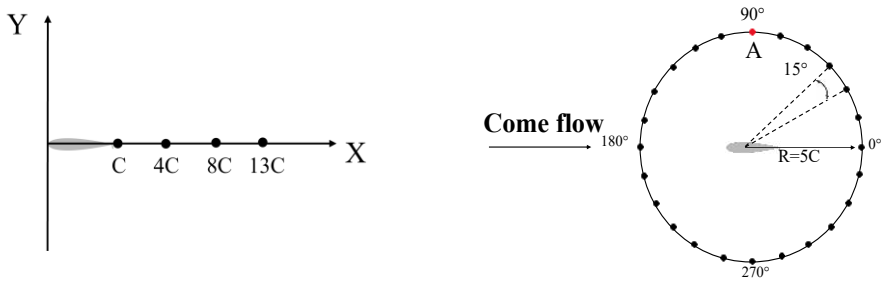

Fig.10. Distribution of acoustic monitoring points

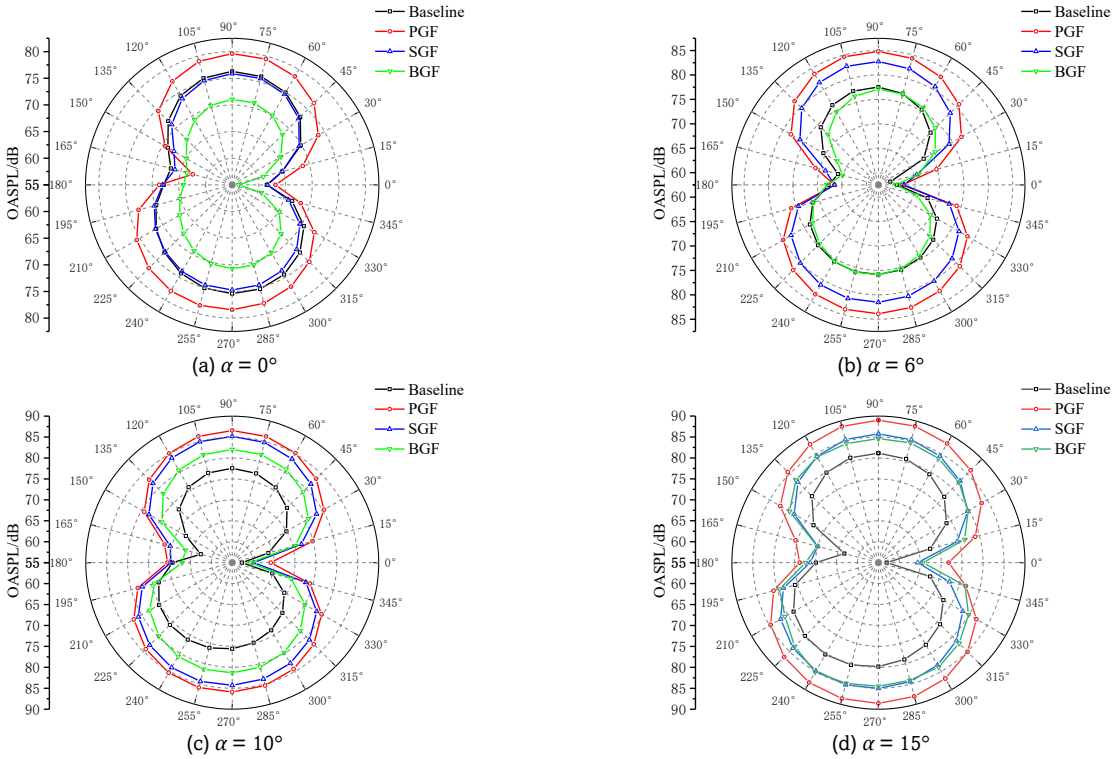

Fig.11. OASPL directivity distributions at different angles of attack

demonstrates prominent dipole-like patterns.The sound pressure level is lowest in the chordwise orientation and reaches a maximum in the direction perpendicular to the chord line.

At α = 0°(Fig. 11a), each configuration displays a classic symmetrical "figure-eight" radiation pattern. The PGF configuration increases noise levels in most radiation directions, specifically by 3.5 dB and 3 dB at 90° and 270°, respectively. Compared to the PGF, the BGF configuration demonstrates superior noise reduction across all azimuthal angles, with a maximum OASPL reduction of approximately 8 dB (a reduction rate of 10.7%). The SGF also exhibits a degree of noise suppression, with its overall directivity curve situated below that of the Baseline.

As the α increases to 6° (Fig. 10b), the global noise level rises as both leading-edge and trailing-edge noise sources intensify. The SGF configuration exhibits a noise level 5.2 dB higher than that of the baseline case, corresponding to an increase of approximately 6.7%.. In contrast, the BGF maintains the lowest noise profile, with a more pronounced sound pressure level reduction in the primary radiation directions, further validating its noise reduction potential at moderate angles of attack.

When α > 10° (Fig. 11c and 11. d) the noise levels further intensify, with all flap-equipped airfoils exhibiting higher noise than the Baseline. While the performance disparities among the four configurations become more prominent, both the BGF and SGF still demonstrate noise-mitigation effects relative to the PGF. Specifically, the BGF achieves attenuation of the SPL in all radiation directions, while the SGF maintains a noise reduction advantage, albeit less effective than the BGF. In summary, the OASPL of the airfoil increases as the angle of attack rises. Among the flap configurations investigated in this study, the BGF maintains effective noise reduction performance at low to moderate angles of attack. Its noise reduction capability is most pronounced at α = 0°; however, as the angle of attack increases, the noise reduction effect diminishes, and by α = 15°, it completely loses its effectiveness.. The flap configurations substantially influence the turbulent structures in the wake region, leading to noticeable differences in the radiated aerodynamic noise. Figure.12 presents the OASPL distributions

Table 3
OASPL results and relative changes Δ for different configurations compared to the baseline airfoil at pont A.

AoA	Baseline OASPL /dB	PGF Δ OASPL /dB	SGF Δ OASPL /dB	BGF Δ OASPL /dB
0°	76.3	+3.5	-0.4	-4.6
6°	77.5	+7.3	+5.2	-0.4
10°	77.6	+9.0	+7.5	+7.4
15°	81.2	+7.8	+4.5	+4.2

at three downstream monitoring locations (x/c = 4, 8 and 13) for the Baseline, PGF, SGF, and BGF airfoils under four angles of attack (0°, 6°, 10°and 15°). In general, the wake noise decreases progressively with downstream distance for all configurations. However, the attenuation rate and overall noise level vary significantly among the different flap geometries and operating conditions.

At low and moderate angles of attack (0°, 6°and 10°), the PGF configuration consistently produces the highest OASPL values at nearly all monitoring positions, suggesting that the PGF intensifies wake turbulence and enhances noise generation. Compared with the Baseline airfoil, the SGF generally provides moderate noise reduction, particularly in the mid- and far-wake regions, although its effectiveness is relatively limited. At x/c = 4, the BGF reduces the OASPL by approximately 5 dB, 10 dB, and 3–4 dB at α = 0°, 6°and 10°, respectively, relative to the Baseline case. The reduction remains evident further downstream, at (x/c = 8) and (13), where the BGF maintains lower overall noise levels than the other flap configurations.

As the angle of attack increases to 15°, the wake-noise characteristics change noticeably. The PGF still exhibits the strongest noise amplification. The SGF shows a certain degree of improvement over the PGF but remains higher than the Baseline at several locations. In contrast to its superior low-angle performance, the BGF no longer achieves overall noise suppression at α = 15°. Although it still maintains relatively low OASPL levels in the near wake, the OASPL in the downstream region increases and even exceeds that of the Baseline and SGF configurations. This behavior suggests that the bionic curved serration becomes less effective under large-angle separated-flow conditions, where intensified vortex interactions and large-scale wake unsteadiness may dominate the acoustic response. Overall, the results indicate that the BGF provides the effective wake-noise suppression under attached or mildly separated flow conditions, whereas its acoustic advantages diminish under high-angle-of-attack conditions with stronger flow separation.

Fig.13 illustrates the acoustic spectral characteristics at Monitoring Point A for the four airfoil configurations under different angles of attack. At $\alpha = 0°$, the PGF exhibits an increase in noise levels in comparison with the baseline case within both the low-frequency (<128 Hz) and mid-frequency (128–1024 Hz) intervals.. Furthermore, compared to the peak sound pressure level of 59 dB at 778 Hz observed for the PGF, the maximum SPL of the BGF is reduced by 4 dB, effectively lowering overall noise intensity.

As the angle of attack increases to 6°, 10°and 15°, the tonal "peak" characteristics in the spectra weaken, and the noise profiles shift toward broadband characteristics. For the flapped airfoils, the intensification of broadband noise may be attributed to the massive separation of vortex structures on the suction surface. Compared to both the PGF and SGF, the BGF

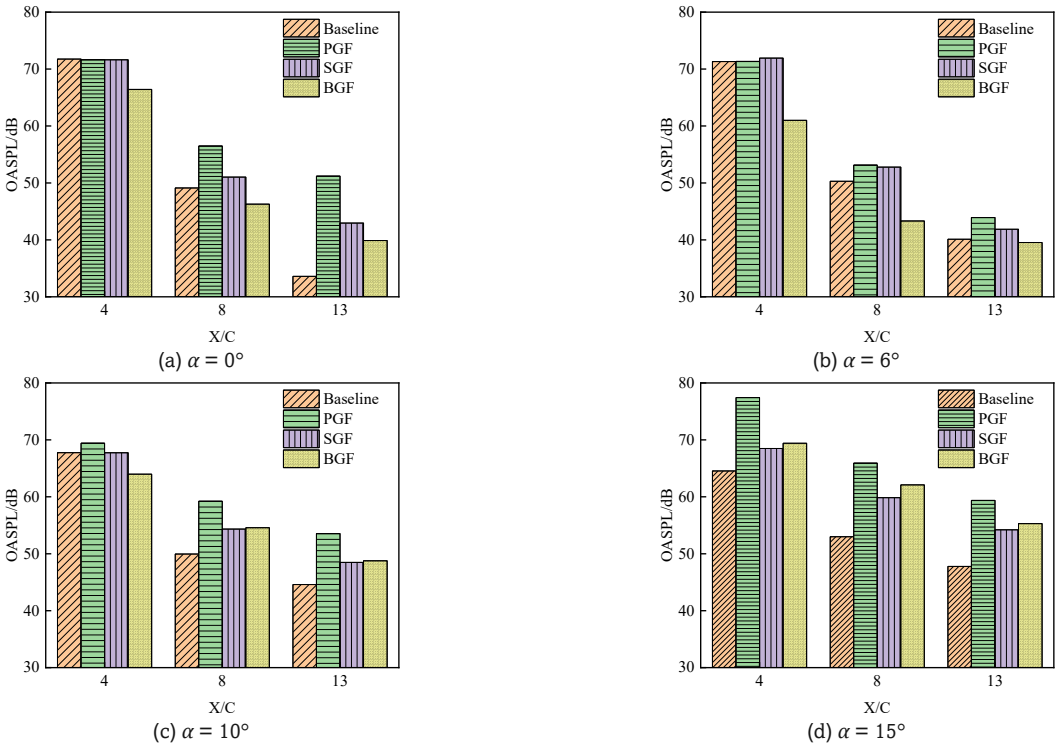

(a) $\alpha = 0°$ (b) $\alpha = 6°$
(c) $\alpha = 10°$ (d) $\alpha = 15°$

Fig.12. Noise distribution in the airfoil wake

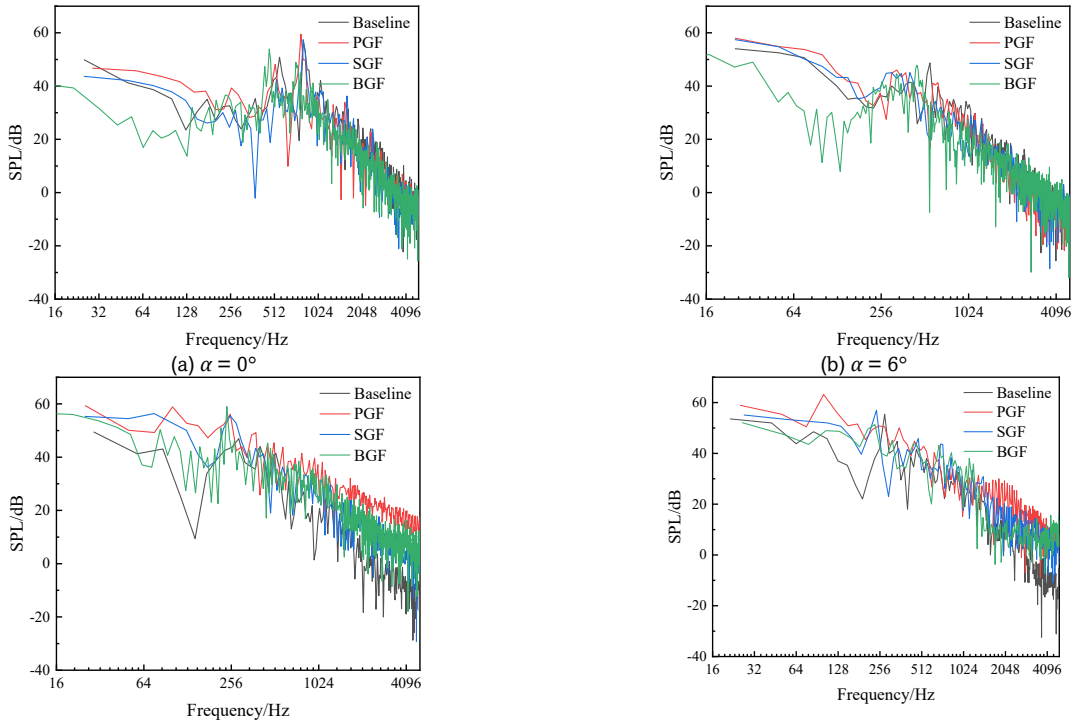

Fig.13. Frequency spectrum at monitoring point A

effectively suppresses noise intensity within the low-to-mid frequency range, a finding that is consistent with the noise directivity patterns presented in Fig.11. This conclusion is consistent with Zhang's research findings (Zhang,2024). To further evaluate the robustness of the proposed flap configurations under different operating conditions, a Reynolds-number sensitivity analysis was conducted. Fig.14 presents the variations in the OASPL of the Baseline, PGF, SGF, and BGF airfoils at Re=7×10^4, 1.4×10^5, and 2.1×10^5, and an angle of attack of 0°.

In general, the OASPL of all configurations increases with Reynolds number, indicating that intensified turbulent fluctuations and enhanced vortex interactions at higher inflow velocities contribute to stronger aerodynamic noise radiation. Among the investigated configurations, the PGF consistently exhibits the highest OASPL across the entire Reynolds-number range,. The SGF shows a moderate reduction in noise compared with the PGF, particularly at low Reynolds numbers; however, its acoustic advantage gradually diminishes as the Reynolds number increases. In contrast, BGF exhibits better acoustic performance at low Reynolds numbers and medium Reynolds numbers of 7×10^4 and 1.4×10^5.As the Reynolds number further increases to 2.1×10^5, the noise-reduction capability of the BGF becomes weaker, and the corresponding OASPL approaches that of the SGF configuration. Nevertheless, the BGF still exhibits lower overall noise levels than the PGF over the entire Reynolds-number range, indicating that the proposed bionic configuration retains a certain degree of aeroacoustic optimization capability under varying inflow conditions.

3.3 Analysis of Noise Reduction Mechanisms

Fig.15 shows the spanwise correlation coefficient (Rpp) distributions of the investigated airfoils. The BGF configuration exhibits spanwise decorrelation characteristics. At

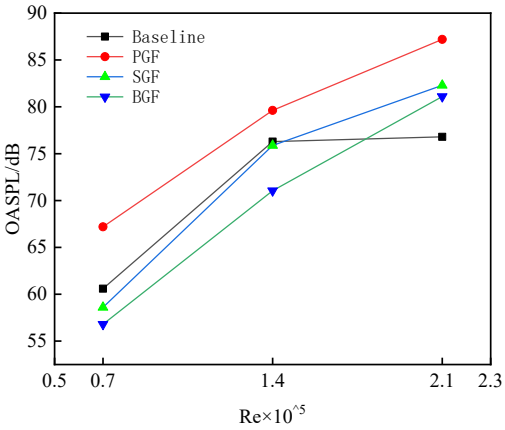

Fig.14. Effect of Reynolds number on the OASPL

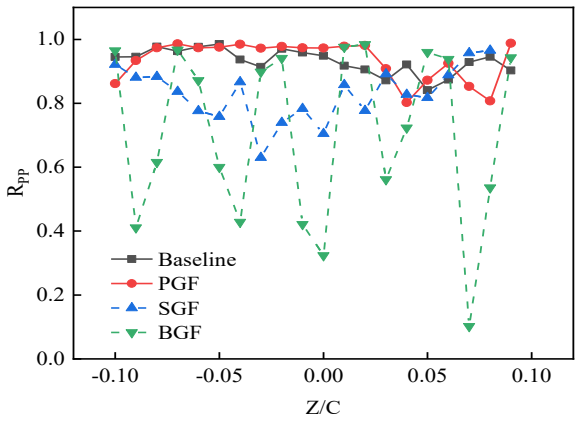

Fig.15. Spanwise correlation of the investigated airfoils

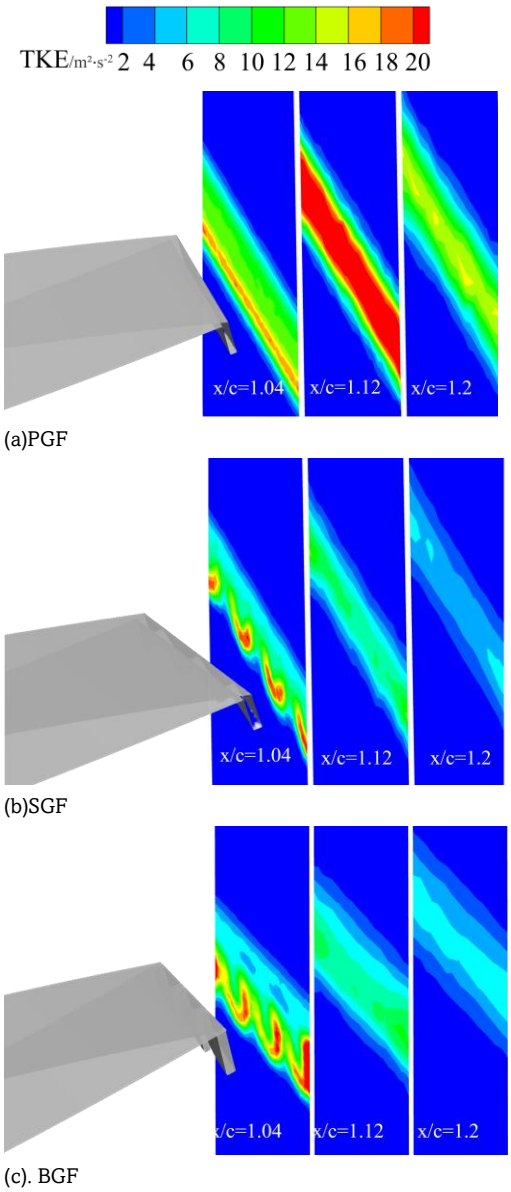

Fig.16. Wake TKE distribution

multiple spanwise locations, Rpp drops sharply to minimum values between approximately 0.1 and 0.4, displaying pronounced periodic fluctuations along the span. These intense correlation oscillations reflect the strong three-dimensional geometric features introduced by the BGF, which trigger additional acoustic energy dissipation within the wake vortices.

Among the configurations, the spanwise correlation of trailing-edge pressure fluctuations is most strongly influenced by the baseline and PGF cases, followed by the SGF, with the BGF exhibiting the weakest correlation. This reduction in spanwise correlation observed for the BGF case serves to suppress the formation of large-scale coherent turbulent structures.This mechanism explains why the BGF achieves a more substantial reduction in OASPL over the same propagation distance. Liu also reached a similar conclusion, indicating that biomimetic trailing edges can reduce spanwise correlation (Liu,2022).

Fig.16 displays the streamwise distributions of TKE in the wake of the four airfoil configurations at x/c = 1.04, 1.12, and 1.2. For the PGF, the TKE distribution in the wake is relatively uniform along the span. In contrast, the TKE distributions for

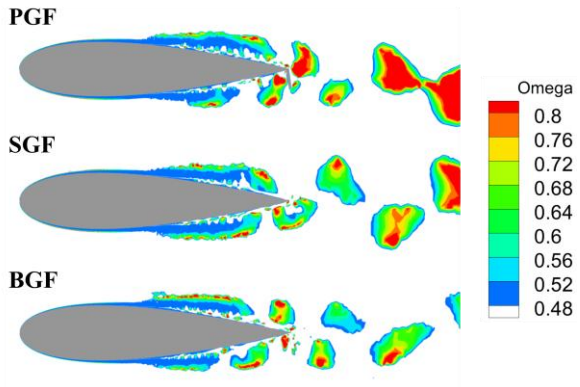

Fig.17. Comparison of cross-sectional vorticity intensity

the SGF and BGF exhibit a periodic pattern closely correlated with their flap geometries, indicating more intense energy exchange in the vicinity of the serrations. The PGF generates larger turbulent structures in the wake, resulting in elevated TKE levels. Combined with the visualizations in Fig.17, it can be inferred that the SGF and BGF decompose large-scale vortices into smaller-scale eddies, thereby effectively suppressing the turbulent kinetic energy.

Fig.17 illustrates the vortex structures in the flow fields of the three flap-equipped airfoils at α = 0°. As the airflow passes over the airfoil, a series of vortex clusters form near the suction surface and around the flaps, subsequently propagating downstream. Vortex structures emerge at 50\%c on the suction surface, separated at the trailing edge. Notably, the vortex threshold intensity and spatial extent of the BGF are smaller than those of the PGF.

The curved bionic geometry produces different adverse pressure gradients along the spanwise direction, resulting in desynchronized vortex shedding. This spatial variation dictates that vortex shedding is no longer synchronized along the trailing edge; instead, a significant phase lag is introduced between adjacent spanwise segments.Such spanwise "disorder" or decoherence provides a fundamental physical explanation for the reduction in the spanwise correlation coefficient Rpp mentioned previously. From an aeroacoustic perspective, when the surface pressure fluctuations at various spanwise locations are no longer superimposed in a constructive or synchronous manner, the intensity of the dipole source is effectively

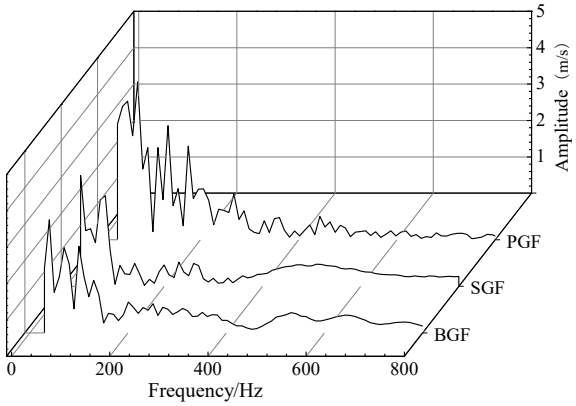

Fig.18. Velocity pulsation spectrum at the trailing edge

attenuated. Consequently, the constructive interference that typically characterizes noise radiation from straight edges is disrupted, leading to a considerable drop in the far-field OASPL radiation. This mechanism yields a optimization of acoustic emission characteristics.

Figure 18 presents the velocity fluctuation spectra at the trailing-edge monitoring point under an angle of attack of 0°. The dominant low-frequency peaks are associated with the large-scale vortex shedding dynamics in the wake region near the trailing edge.The vortex shedding frequency of the PGF exhibits discrete characteristics, while the main peak value of the velocity pulsation of the modified blade decreases; The dominant wake fluctuation frequencies of the PGF, SGF, and BGF are approximately 72.2 Hz, 30.0 Hz, and 40.2.0 Hz, respectively.

In combination with the vorticity contours shown in Fig. 17, these results suggest that the serrated flap geometry modifies the unsteady wake structures and weakens the spanwise coherence of large-scale vortices, thereby affecting the wake evolution and contributing to aerodynamic noise suppression.

4. Conclusions

This study investigates the noise reduction performance of a bionic curved serrated flap inspired by owl wing structures. Employing a hybrid numerical approach combining IDDES and the FW-H acoustic analogy, the aerodynamic performance and aeroacoustic behavior of four airfoil—Baseline, PGF, SGF, and BGF—were simulated under conditions ranging from low angles of attack to the stall angle of attack. The primary conclusions are summarized as follows:

1. The implementation of Gurney flaps, whether in their traditional SGF form or the bionic BGF variant, leads to a marked increase in both the lift coefficient and lift-to-drag ratio. This aerodynamic modification is achieved by amplifying the pressure difference between the suction and pressure sides, along with an elevation of the leading-edge suction peak. However, the penalty for this substantial lift enhancement is a forward shift in the stall angle of attack by roughly 3°.
2. Compared to the PGF configuration, the BGF exhibits lower overall sound pressure levels across the investigated acoustic radiation directions. Relative to the baseline airfoil, the BGF maintains an effective noise-reduction capability at low angles of attack ($\alpha < 6°$), with the optimal suppression occurring at $\alpha = 0°$ where the maximum sound pressure level is reduced by approximately 4.6 dB. Although this mitigation effect gradually diminishes with the increment of the angle of attack, the BGF consistently outperforms the traditional serrated flap prior to the stall angle, while preserving the characteristic dipole directivity typical of airfoil aerodynamic noise.
3. Analysis of the spanwise correlation, wake turbulent kinetic energy (TKE), and wake vortex structures further clarifies the underlying noise-reduction mechanism of the bionic airfoil. The introduction of serrations to the conventional Gurney flap decreases the spanwise coherence of flow structures., effectively suppresses the TKE at the trailing edge, and mitigates vortex intensity. The intensity of wake shedding vortices and turbulence for the BGF is lower than that of the other two flap configurations.

Overall, the present numerical results indicate that the proposed bionic curved serrated flap has potential for reducing airfoil aerodynamic noise under low-angle-of-attack and different flow rates tested conditions. Nevertheless, further investigations under broader operating conditions and additional experimental validation are still required to assess its robustness and practical applicability.

References

Amini, Y., Emdad, H., & Farid, M. (2015). Adjoint shape optimization of airfoils with attached Gurney flap. *Aerospace Science and Technology*, 41, 216–228. https://doi.org/10.1016/j.ast.2014.12.023

Amiet, R. K. (1975). Acoustic radiation from an airfoil in a turbulent stream. *Journal of Sound and Vibration*, 41, 407–420. https://doi.org/10.1016/S0022-460X(75)80105-2

Asada, K., & Kawai, S. (2018). Large-eddy simulation of airfoil flow near stall condition at Reynolds number 2.1×10^6. *Physics of Fluids*, 30(8), 085103. https://doi.org/10.1063/1.5037278

Avallone, F., Probsting, S., & Ragni, D. (2016). Three-dimensional flow field over a trailing-edge serration and implications on broadband noise. *Physics of Fluids*, 28(11), 117101. https://doi.org/10.1063/1.4966633

Brooks, T. F., Pope, D. S., & Marcolini, M. A. (1989). Airfoil self-noise and prediction. *NASA Reference Publication*, 1218. https://ntrs.nasa.gov/citations/19890016302

Chen, H., Yuan, X., Bi, L., (2020). Simulation of separation flow based on RANS/LES hybrid method. *Acta Aeronautica et Astronautica Sinica*, 41(8), 183–194. https://doi.org/10.7527/S1000-6893.2020.23642

Chen, K., Feng, W., Zhang, Z. (2024). Study on aerodynamic noise of airfoil with curved serration trailing edge based on characteristics of owl wing. *Acta Energiae Solaris Sinica*, 45(4), 272–279. https://doi.org/10.19912/j.0254-0096.tynxb.2022-1926

Chen, X., Zheng, L., Cai, G., Qi, X., He, J. (2025). Global perspectives on wind energy innovation: Policy impacts and component-level analysis. *Energy*, 319, 135000. https://doi.org/10.1016/j.energy.2025.135000

Chong, T. P., Vathylakis, A., Joseph, P. F., Gruber, M. (2013). Self-noise produced by an airfoil with nonflat plate trailing-edge serrations. *AIAA Journal*, 51(11), 2665–2677. http://dx.doi.org/10.2514/1.J052344

Colonius, T., & Lele, S. K. (2004). Computational aeroacoustics: progress on nonlinear problems of sound generation. *Progress in Aerospace Sciences*, 40(6), 345–416. https://doi.org/10.1016/j.paerosci.2004.09.001

Feng, W., Chen, K., & Gui, H. (2023). Aerodynamic noise reduction based on bionic blades with non-smooth leading edges and curved serrated trailing edges. *Journal of Applied Fluid Mechanics*, 16(7), 1402–1413. https://doi.org/10.47176/jafm.16.07.1660

Fujisawa, N., Shibuya, S., Nashimoto,A., Takarno, T (2001). Aerodynamic noise and flow visualization around twodimensional airfoil. *Transactions of the Visualization Society of Japan*.21(9), 123-129. https://doi.org/10.3154/TVSJ.21.123

Howe, M. S. (1991). Noise produced by a sawtooth trailing edge. *The Journal of the Acoustical Society of America*, 90(1), 482–487. https://doi.org/10.1121/1.401273

Jacobs, E. N., & Sherman, A. (1937). Airfoil section characteristics as affected by variations of the Reynolds number. *NACA Technical Report*, 586, 227–267. https://ntrs.nasa.gov/citations/19930091652

Kim, H. J., Lee, S., & Fujisawa, N. (2006). Computation of unsteady flow and aerodynamic noise of NACA0018 airfoil using large-eddy simulation. *International Journal of Heat and Fluid Flow*, 27(2), 229–242. https://doi.org/10.1016/j.ijheatfluidflow.2005.08.007

Kong, D., Liang, A., Chu, J., (2015) Study on Mechanism of Silent Flight of Owls. *Applied Physics*, 05(11), 137-146. https://doi.org/10.12677/APP.2015.511019

Li, S., Li, Y., Yang, C., Wang, Q., Zhao, B., Li, D., Zhao, R., Ren, T., Zheng, X., Gao, Z., Xu, W. (2021). Experimental investigation of solidity and other characteristics on dual vertical axis wind turbines in an urban environment. *Energy Conversion and Management*, 229(1), 113689. https://doi.org/10.1016/j.enconman.2020.113689

Liu, C. (2020). Liutex-third generation of vortex definition and identification methods. *Acta Aerodynamica Sinica*, 38(3), 413–431. https://doi.org/10.7638/kqdlxxb-2020.0015

Liu, J., Lin, H., & Zhang, J. (2019). Review on the technical perspectives and commercial viability of vertical axis wind turbines. *Ocean Engineering*, 182(15), 608–626. https://doi.org/10.1016/j.oceaneng.2019.04.086

Liu, T., & Montefort, J., (2007). Thin-airfoil theoretical interpretation for gurney flap lift enhancement. *Journal of Aircraft*, 44(2), 667–771. https://doi.org/10.2514/1.24423

Liu, X., Tang, H., Wang, X. (2012). Noise-reduction mechanism of bionic coupling blade based on the trailingedge of goshawk wing. *Academic Journal of Xi'an Jiaotong University*, 46(1), 35–41. https://doi.org/10.7638/kqdlxxb-2017.0162

May, R., Masden, E. A., Bennet, F., Perron, M (2019). Considerations for upscaling individual effects of wind energy development towards population-level impacts on wildlife. *Journal of Environmental Management*, 230, 84–93. https://doi.org/10.1016/j.jenvman.2018.09.062

Menter, F. R. (1994). Two-equation eddy-viscosity turbulence models for engineering applications. *AIAA Journal*, 32(8), 1598–1605. https://doi.org/10.2514/3.12149

Meyer, R., Hage, W., & Bechert, D. W. (2006). Drag reduction on Gurney flaps by three-dimensional modifications. *Journal of Aircraft*, 43(1), 132–140. https://doi.org/10.2514/1.14294

Oerlemans, S., Fisher, M., Maeder, T., Kogler, K. (2009). Reduction of wind turbine noise using optimized airfoils and trailing-edge serrations. *AIAA Journal*, 47(6), 1470–1481. https://doi.org/10.2514/1.38888

Piorkowski, M. D., Farnsworth, A. J., Fry, M., Rohrbaugh, R.W., Fitzpatrick, J.W., Rosenberg, K.V. (2012). Research priorities for wind energy and migratory wildlife. *Journal of Wildlife Management*, 76(3), 451–456. https://doi.org/10.1002/jwmg.327

Powell, A. (1964). Theory of vortex sound. T*he Journal of the Acoustical Society of America*, 36(1), 177–195.https://doi.org/10.1121/1.1918931

Si, J., Ai, L., & Qiu, C. (2024). Status and prospect of China's wind power development in 2023. *Water Power*, 50(12), 1–4. https://link.cnki.net/urlid/11.1845.TV.20241009.1543.004

Song, D., Yang, Y., Zheng, S., Deng, X., Yang, J., Su, M., Tang, W., Yang, X., Huang, L. (2020). New perspectives on maximum wind energy extraction of variable-speed wind turbines using previewed wind speeds. *Energy Conversion and Management*, 206, 112496. https://doi.org/10.1016/j.enconman.2020.112496

Sun, X., Zhang, L., Huang, D., Zheng, Z. (2017). New insights into aerodynamic characteristics of oscillating wings and performance as wind power generator. *International Journal of Energy Research*, 42(2), 776–789. https://doi.org/10.1002/er.3865

Wang, J. J., Li, Y. C., & Choi, K. S. (2008). Gurney flap—lift enhancement, mechanisms and applications. *Progress in Aerospace Sciences*, 44(1), 22–47. https://doi.org/10.1016/j.paerosci.2007.10.001

Wang, L., & Liu, X. M. (2022). Aeroacoustic investigation of asymmetric oblique trailing-edge serrations enlighted by owl wings. *Physics of Fluids*, 34(1), 015113. https://doi.org/10.1063/5.0076272

Wilbur, M. L., Mistry, M. P., Lorber, P. F., Blackwell, R., Barbarino, S., Lawrence, T.H., Arnold, T.P. (2018). Rotary wings morphing technologies: State of the art and perspectives. *Morphing Wing Technologies*, 759–797. https://doi.org/10.1016/B978-0-08-100964-2.00024-1

Wu, X., Hu, W., Huang, Q., Chen, C., Jacobson, M.Z., Chen, Z. (2020). Optimizing the layout of onshore wind farms to minimize noise. *Applied Energy*, 267(1), 114896. https://doi.org/10.1016/j.apenergy.2020.114896

Yan, Y., Avital, E., William, J., Cui, J. (2020). Performance improvements for a vertical axis wind turbine by means of Gurney flap. *Journal of Fluids Engineering*, 142(2), 021205. https://doi.org/10.1115/1.4044995

Yang, J., Yang, A., Chen, E., (2017). Numerical research on aerodynamic characteristics and flow fields of airfoil with serrated trailing edge. *Journal of Aerospace Power*, 32(4), 900–908. https://doi.org/10.13224/j.cnki.jasp.2017.04.015

Yang, Z., Li, X., Zhang, K., (2025) Numerical study on benefits of curved serrations upon suppressing turbulent boundary layer trailing-edge noise. Physics Letters A, 530,130131. https://doi.org/10.1016/j.physleta.2024.130131

Yu, Y., Chen, L., Zheng, Z., (2022). Effect of serrated gurney flap on NACA0018 airfoil wake with liutex identification method. *Acta Energiae Solaris Sinica*, 43(10), 210–217. https://doi.org/10.19912/j.0254-0096.tynxb.2021-0343

Zhang, B., Yang, P., He, C.(2024). Study on the aerodynamic and noise effects of serrated structure on NACA2418 flap airfoil. *Modeling and Simulation*, 13(1), 11. https://doi.org/10.12677/MOS.2024.131092

Zhang, N., Jiang, J. X., Gao, B., Liu, X., Ni, D. (2020). Numerical analysis of the vortical structure and its unsteady evolution of a centrifugal pump. *Renewable Energy*, 155, 748–760. https://doi.org/10.1016/j.renene.2020.03.182